Chemical Engineering Journal 404 (2021) 126573

Contents lists available at ScienceDirect

Chemical Engineering Journal

journal homepage: www.elsevier.com/locate/cej

# Reactor modelling and design for sorption enhanced dimethyl ether synthesis

Simone Guffanti[a], Carlo Giorgio Visconti[a], Jasper van Kampen[b], Jurriaan Boon[b], Gianpiero Groppi[a,*]

[a] Laboratory of Catalysis and Catalytic Processes, Dipartimento di Energia, Politecnico di Milano via La Masa 34, 20156 Milano, Italy
[b] Biomass and Energy Efficiency, TNO Energy Transition, P.O. Box 15, 1755ZG Petten, the Netherlands

## HIGHLIGHTS

- Model analysis of fixed bed reactor for Sorption Enhanced DiMethyl Ether Synthesis.
- Model validation with experimental data from bench scale reactor.
- SEDMES ensures high $CO_x$ conversion and DME selectivity for any $CO/CO_2$ feed ratio.
- Larger diameter tubes than in conventional direct DME synthesis can be adopted in SEDMES.

## GRAPHICAL ABSTRACT

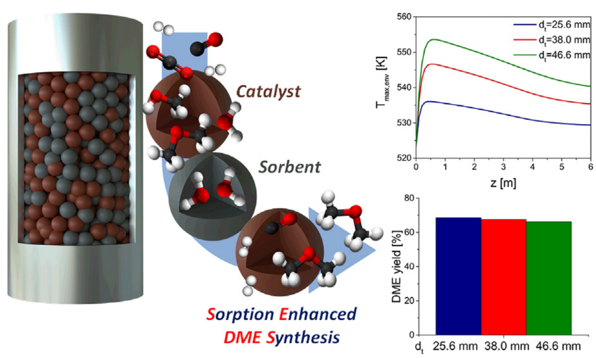


## ARTICLE INFO

*Keywords:*
Sorption enhancement
Dimethyl ether direct synthesis
Fixed bed reactors
Reactor modelling
Reactor design

## ABSTRACT

Sorption Enhanced DiMethyl Ether Synthesis (SEDMES) is a promising option to overcome thermodynamic limitations of conventional DME production processes. In this work a 2D + 1D heterogeneous dynamic model of the reaction/adsorption step in a tube of an externally cooled multitubular fixed bed SEDMES reactor is developed in order to investigate the effect of design and operating parameters on thermal behavior and DME yield performances of the reactor. The model is validated by comparison with experimental results from a bench scale unit, including the dynamics of the outlet composition and the temperature trajectories in different points along the axial coordinate. Simulations with the validated model address the effect of the $CO/CO_2$ ratio in the feed. The results confirm that, thanks to the effective in-situ $H_2O$ removal, the DME yield performances (65–70% in this work) of SEDMES are poorly sensitive on the $CO/CO_2$ ratio. Accordingly, on increasing the $CO_2$ content in the feed, SEDMES provides larger advantages with respect to conventional DME direct synthesis. Calculations of maximum temperatures achieved along the axial coordinate show that catalyst thermal stress in the hottest inlet zone of the SEDMES reactor slightly increases with the CO content in the feed due to faster kinetics of the DME production reactions. However, thanks to the dilution effect provided by the adsorption material, maximum bed temperature keeps ~ 20–30 K below the catalyst stability limit reported in the literature (573 K). Accordingly, larger tube diameters (up to 46.6 mm) than in conventional reactors for the direct synthesis of DME can be adopted with less than 2% loss in DME yield.

* Corresponding author.
*E-mail address:* gianpiero.groppi@polimi.it (G. Groppi).

https://doi.org/10.1016/j.cej.2020.126573
Received 4 May 2020; Received in revised form 3 August 2020; Accepted 5 August 2020
Available online 09 August 2020

**Notation**

| | |
|---|---|
| $a_v$ | Solid specific surface area per unit volume [$m^2/m^3$] |
| $C_p$ | Gas mixture specific heat [J/kg/K] |
| $C_i$ | Molar concentration of species i [$mol/m^3$] |
| $C_{tot}$ | Total molar concentration [$mol/m^3$] |
| $d_p$ | Pellet diameter [m] |
| $d_t$ | Tube internal diameter [m] |
| $D_{ae,i}$ | Effective axial dispersion of species i [$m^2/s$] |
| $D_{eff,i}$ | Effective diffusion coefficient of species i in solid [$m^2/s$] |
| $D_{re,i}$ | Effective radial dispersion of species i [$m^2/s$] |
| $D_{ij}$ | Binary diffusion coefficient of species i in species j [$m^2/s$] |
| $D_{k,i}$ | Knudsen diffusion coefficient of species i [$m^2/s$] |
| $D_{mix,i}$ | Molecular diffusion coefficient of species i [$m^2/s$] |
| $f_i$ | Fugacity of species i [bar] |
| $F_i$ | Molar flow rate of species i per unit area [mol/ $m^2/s$] |
| $F_{tot}$ | Total molar flow rate per unit area [$mol/m^2/s$] |
| $h_{gs}$ | Gas-solid heat transfer coefficient [$W/m^2/K$] |
| $h_w$ | Wall heat transfer coefficient [$W/m^2/K$] |
| $h_{w,conv}$ | Wall convective heat transfer coefficient [$W/m^2/K$] |
| $k_1$ | Kinetic constant of CO hydrogenation to methanol [mol/ $kg_{cat}/s/bar^{3/2}$] |
| $k_2$ | Kinetic constant of reverse water gas shift [mol/$kg_{cat}$/s/ bar] |
| $k_3$ | Kinetic constant of $CO_2$ hydrogenation to methanol [mol/ $kg_{cat}$/s/ $bar^{3/2}$] |
| $k_4$ | Kinetic constant of methanol dehydration to dimethyl ether [mol/$kg_{cat}$/s] |
| $k_{m,i}$ | Gas-solid mass transfer coefficient of species i [m/s] |
| $K_{CH3OH}$ | Adsorption constant of methanol on dehydration catalyst [$m^3$/mol] |
| $K_{CO}$ | Adsorption constant of CO on methanol synthesis catalyst [$bar^{-1}$] |
| $K_{CO2}$ | Adsorption constant of $CO_2$ on methanol synthesis catalyst [$bar^{-1}$] |
| $K_{eq,j}$ | Equilibrium constant of reaction j |
| $K_{H2O}$ | Adsorption constant of $H_2O$ on dehydration catalyst [$m^3$/ mol] |
| $K_{H2O/H2}$ | Adsorption group of $H_2O/H_2$ on methanol synthesis catalyst [$bar^{-1/2}$] |
| $K_{LDF}$ | Linear driving force coefficient [$s^{-1}$] |
| $K_\Phi$ | Product of fugacity coefficients [-] |
| $L_t$ | Tube length [m] |
| $MW_i$ | Molar weight of species i [kg/mol] |
| $N_C$ | Number of components [-] |
| $N_{cat}$ | Number of catalyst phases [-] |
| $N_R$ | Number of reactions [-] |
| Nu | Nusselt number [-] |
| P | Pressure [Pa] |
| Pr | Prandtl number [-] |
| q | Adsorbent water load [mol/kg] |
| $q_{sat}$ | Adsorbent saturation water load [mol/kg] |
| R | Reactor radial coordinate [m] |
| $r_p$ | Pellet radius [m] |
| $r_{pore}$ | Pore radius [m] |
| R | Gas universal constant [J/mol/K] |
| $R_j$ | Rate of reaction j [mol/kg/s] |
| Re | Reynolds number [-] |
| $S_p$ | Geometric pellet surface area [$m^2$] |
| Sc | Schmidt number [-] |
| Sh | Sherwood number [-] |
| t | Time [s] |
| T | Temperature [K] |
| $T_{cool}$ | Coolant temperature [K] |
| $v_{gas}$ | Gas velocity [m/s] |
| $V_p$ | Pellet volume [$m^3$] |
| $V_t$ | Reactor volume [$m^3$] |
| x | Pellet radial coordinate [m] |
| $y_i$ | Molar fraction of species i [-] |
| $Y_{CDME}$ | Normalized dimethyl ether outlet carbon flow rate [-] |
| $Y_{DME}$ | Dimethyl ether carbon yield [-] |
| z | Reactor axial coordinate [m] |

*Greek letters*

| | |
|---|---|
| $\Delta H_{ads}$ | Heat of adsorption [J/mol] |
| $\Delta H_{r,j}$ | Heat of reaction j [J/mol] |
| $\varepsilon_b$ | Bed void fraction [-] |
| $\varepsilon_p$ | Particle porosity [-] |
| $\eta_j$ | Catalyst effectiveness factor of reaction j [-] |
| $\lambda_{ax}$ | Effective axial thermal conductivity [W/m/K] |
| $\lambda_{rad}$ | Effective radial thermal conductivity [W/m/K] |
| $\lambda_{gas}$ | Gas mixture thermal conductivity [W/m/K] |
| $\lambda_s$ | Solid thermal conductivity [W/m/K] |
| $\nu_{ij}$ | Stoichiometric coefficient of species i in reaction j [-] |
| $\xi_{ads}$ | Volumetric fraction of adsorbent [-] |
| $\xi_{cat}$ | Volumetric fraction of catalyst [-] |
| $\xi_k$ | Volumetric fraction of catalyst phase k [-] |
| $\rho$ | Density [$kg/m^3$] |
| $\sigma_{react}$ | Extent of reaction [mol] |
| $\tau$ | Tortuosity [-] |
| $\upsilon_i$ | Diffusional volume of species i [$cm^3$/mol] |
| $\Phi_i$ | Fugacity coefficient of species i [-] |

*Superscripts and subscripts*

| | |
|---|---|
| 0 | Reactor inlet condition |
| ads | Adsorbent phase |
| ae | Effective axial |
| av | Average |
| ax | Axial |
| b | Bed |
| cat | Catalyst phase |
| cool | Coolant |
| eff | Effective |
| end | End of reaction/adsorption step |
| gas | Gas phase |
| i | i-species (i = CO, $CO_2$, $H_2$, $H_2O$, MeOH, DME, $N_2$) |
| int | Intraparticle |
| j | j-reaction |
| k | k-catalyst phase (k = MeOH, DME) |
| p | Pellet |
| pa | Spherical particle with equal surface area |
| pe | Equivalent spherical particle |
| pv | Spherical particle with equal volume |
| rad | Radial |
| re | Effective radial |
| s | Referred to the solid phase |
| t | Referred to the tube |
| tot | Total |
| w | Referred to the tube wall |

## 1. Introduction

Dimethyl ether (DME) is an environmentally-friendly chemical (not toxic, not cancerogenic and not ozone-depleting) commonly used as propellant, that is also accounted as a promising alternative fuel with many possible applications: clean diesel for compression-ignition engines, substitute for LPG, fuel for power generation in turbines and hydrogen storage for fuel cells [1–6]. Currently, DME is industrially obtained from syngas (CO, $CO_2$ and $H_2$ mixture) through a consecutive two steps catalytic process: the methanol synthesis, that uses Cu/ZnO/$Al_2O_3$ (CZA) catalyst [7], followed by the methanol dehydration, performed with acid catalysts like γ-alumina, zeolites or silicoaluminophosphates (SAPO) [8]. This process is known as DME indirect synthesis. Another possible synthesis route is the DME direct synthesis, that consists of the integration of methanol synthesis and dehydration reactions in a single reactor by simply mixing pellets providing the two catalytic functions [9] or by coupling them in a single hybrid/bifunctional catalyst [9,10]. The direct process can be represented by four reactions: the methanol synthesis from CO (1), the water gas shift (2), the methanol synthesis from $CO_2$ (3) and the methanol dehydration to DME (4).

$$CO + 2H_2 \leftrightarrow CH_3OH \quad \Delta H_r^0 = -90.5\text{kJ/mol} \tag{1}$$

$$CO + H_2O \leftrightarrow CO_2 + H_2 \quad \Delta H_r^0 = -41.1\text{kJ/mol} \tag{2}$$

$$CO_2 + 3H_2 \leftrightarrow CH_3OH + H_2O \quad \Delta H_r^0 = -49.4\text{kJ/mol} \tag{3}$$

$$2CH_3OH \leftrightarrow CH_3OCH_3 + H_2O \quad \Delta H_r^0 = -23.0\text{kJ/mol} \tag{4}$$

The advantage of coupling methanol synthesis with dehydration in a single reactor is given by the thermodynamic synergy between the two processes, which enhances the equilibrium conversion of reactants [11]. However, in case of a CO rich syngas, $CO_2$ becomes an undesired by-product, due to the WGS equilibrium shift [12,13]. Instead, in case of a $CO_2$ rich feed gas, obtained for example from biomass gasification [14], the synergy progressively fades away as a consequence of the large water production that makes the thermodynamic limitations more stringent [13,15]. Moreover, the large amount of water produced in presence of $CO_2$ hinders the catalytic activity of methanol synthesis catalyst [11,16] and reversibly deactivates the dehydration catalyst [17].

In-situ removal of water is a possible solution to these issues [18], allowing to overcome the thermodynamic limitations, reducing the outlet content of $CO_2$ and preventing catalyst deactivation by water. In principle steam separation enhanced DME synthesis can be obtained using selective membranes [19] or in-situ adsorption [18,20,21]. The membrane separation has the advantage to work at steady-state, while a cyclic regeneration of the adsorbent material is required in reactive adsorption. This second solution is anyway more suitable, since low water partial pressure must be reached in the reactor for a substantial enhancement of the DME synthesis process and water removal in membranes is effective only with a consistent partial pressure gradient (indicatively $>$ 1 bar) [18].

The so called Sorption Enhanced DME Synthesis (SEDMES) comprises the coupling the DME synthesis catalyst (e.g a physical mixture of methanol synthesis and dehydration catalyst or hybrid catalyst) with an adsorbent material with high capacity and selectivity to water adsorption, e.g. LTA zeolites 4A and 3A [22–24]. Despite the potential of steam sorption enhancement has been proved theoretically and experimentally since many years in other water producing equilibrium limited processes like the reverse water gas shift (rWGS) [25], the methanation [26,27] and methanol synthesis [28,29], there is not an extensive literature specifically on SEDMES. A first experimental investigation on the liquid-phase SEDMES has been performed by Kim et al. [30]. Without considering the adsorbent regeneration they observed an effective, but relatively short, enhancement given by the water adsorption. Iliuta et al. [20] theoretically showed the potential of the SEDMES on industrial scale, using an isothermal 1D model of the reactor gas phase coupled with a 1D model of the solid pellets in order to analyze the effect of the composition compared to a conventional process. Recently, van Kampen et al. [18] have shown experimentally that high reactants conversion and carbon selectivity to DME can be obtained with sorption enhancement independently from the feed CO/$CO_2$ ratio. In a following work, van Kampen et al. [21] have analyzed the SEDMES cycle with a 1D heterogeneous model, validated with experimental data, addressing the effects on the process performances of different operating conditions (temperature, pressure, space velocity, adsorbent/catalyst ratio) and pointing out the critical role of the regeneration method: Temperature Swing Adsorption, Pressure Swing Adsorption, Temperature-Pressure Swing Adsorption (TSA, PSA, TPSA). Moreover, the importance of heat management has been pointed out, showing that a strong loss in DME yield is observed when operating under adiabatic conditions instead of isothermal ones, due to the loss of adsorption capacity at increasing temperatures [21].

Accordingly, temperature control is a relevant issue in SEDMES, which in addition to high exothermicity of DME direct synthesis should cope with exothermic water adsorption. Indeed lack of heat management, in addition to cause unfavorable thermodynamic conditions [21,23], may result in catalyst deactivation [16,31].

In this work a mathematical model of the reaction/adsorption step in a single tube of a multitubular reactor is developed aiming at the analysis of the thermal behavior as a key factor for the rational design of an industrial scale SEDMES reactor. The model provides a detailed description of temperature profiles by solving 2D dynamic mass and enthalpy balances of a single tube reactor coupled with 1D pseudo-stationary model of the catalyst pellets, accounting for the intraparticle diffusion limitations. The model, implemented in gPROMS® for the numerical solution, is validated with experimental data of the time evolution of outlet gas composition and axial temperature profile collected in a bench scale unit. Then it is used for the analysis of the thermal behavior of an industrial scale reactor, focusing on the dynamic of the reaction/adsorption step, which is the most demanding cycle step from a temperature control perspective. The effects of different feed CO/$CO_2$ ratios and tube diameters are addressed.

## 2. Methodology

### 2.1. SEDMES reactor model

A heterogeneous two-dimensional dynamic model of a single tube of an externally cooled multi tubular fixed bed reactor has been developed. The model describes the time evolution of concentration and temperature radial and axial profiles of the adsorption/reaction step of a SEDMES cycle. The model includes 2D total mass balance for gas phase, 2D i-species mass (i = CO, $CO_2$, $H_2$, $H_2O$, $CH_3OH$, DME, $N_2$) and energy balances for the gas-phase, catalyst and adsorbent solid phases. Two separate k-catalyst phases, methanol catalyst (MeOH) and dimethyl ether synthesis catalyst (DME), are considered. The intraparticle diffusion limitations in the catalyst particles are accounted coupling the dynamic reactor model with pseudo-stationary 1D mass balances of i-species in isothermal catalyst pellets. The pressure drops in the reactor, evaluated with a 1D momentum balance, are negligible in the investigated range of operating condition. Therefore, isobaric conditions are taken in the simulations. The physical and chemical properties (molecular weight, specific heat, density, viscosity and thermal conductivity) of the reacting mixture are calculated using the gPROMS® Multiflash 4.3 utility tool, while diffusivities, mass and heat transport coefficients are calculated with literature correlations (see Supplementary materials - Section S1).

#### 2.1.1. 2D dynamic mass balances

The total mass balance for the gas phase (eq. (5)), expressed in molar form, consists of four terms: molar capacity, axial convection, mass exchange between gas and k-catalyst phases, mass exchange between the gas and the adsorbent phase.

$$\varepsilon_b \frac{\partial C_{gas,tot}}{\partial t} = -\frac{\partial (C_{gas,tot} v_{gas})}{\partial z} + \sum_k^{N_{cat}} \sum_i^{N_C} a_{v,cat_k} k_{m,cat_k,i} (C_{cat_k,i} - C_{gas,i}) + a_{v,ads} \sum_i^{N_C} k_{m,ads,i} (C_{ads,i} - C_{gas,i}) \tag{5}$$

The solid surface area per unit volume (eq. (6)) depends on the solid phase considered (catalyst or adsorbent) and it is weighted with the volumetric fraction per unit volume $\xi$ related to the specific solid phase ($\xi_{ads} + \xi_{cat} = 1$). The $\xi_k$ refers to the MeOH or the DME catalyst ($\xi_{MeOH} + \xi_{DME} = 1$). This scheme is applied to all the balance equations next.

$$a_{v,ads} = (1 - \varepsilon_b) \xi_{ads} S_{P_{ads}} / V_{P_{ads}}$$

$$a_{v,cat_k} = (1 - \varepsilon_b) \xi_{cat} \xi_k S_{p,cat_k} / V_{p,cat_k} \quad \text{k = MeOH, DME} \tag{6}$$

The i-species gas phase molar balances (eq. (7)) consist of six terms: molar capacity; axial convection; radial and axial molar dispersion; mass transfer between the gas and k-catalyst phases and between the gas and the adsorbent phase.

$$\varepsilon_b \frac{\partial C_{gas,i}}{\partial t} = -\frac{\partial (C_{gas,i} v_{gas})}{\partial z} + D_{re,i} \left( \frac{\partial^2 C_{gas,i}}{\partial r^2} + \frac{1}{r} \frac{\partial C_{gas,i}}{\partial r} \right) + D_{ae,i} \frac{\partial^2 C_{gas,i}}{\partial z^2} + \sum_k^{N_{cat}} a_{v,cat_k} k_{m,cat_k,i} (C_{cat_k,i} - C_{gas,i}) + a_{v,ads} k_{m,ads,i} (C_{ads,i} - C_{gas,i}) \tag{7}$$

The i-species molar balances for the catalyst phase (eq. (8)) consist of three terms: molar capacity; mass transfer between the gas and catalyst phase; reaction consumption/production. Two separate mass balances, one for each k-catalyst phase, are required.

$$(1 - \varepsilon_b) \xi_{cat} \xi_k \varepsilon_{p,cat_k} \frac{\partial C_{cat_k,i}}{\partial t} = a_{v,cat_k} k_{m,cat_k,i} (C_{gas,i} - C_{cat_k,i}) + (1 - \varepsilon_b) \xi_{cat} \xi_k \rho_{cat_k} \sum_j^{N_R} \nu_{ij} R_{j,k}^{av} \tag{8}$$

Assuming ideal selectivity of the adsorbent, the balances for all the i-species except $H_2O$ (eq. (9)) only consider the gas phase within the adsorbent pores and includes the molar capacity term and mass transfer between the external fluid and adsorbent phase.

$$(1 - \varepsilon_b) \xi_{ads} \varepsilon_p \frac{\partial C_{ads,i}}{\partial t} = a_{v,ads} k_{m,ads,i} (C_{gas,i} - C_{ads,i}) \quad i \neq H_2O \tag{9}$$

In the case of the $H_2O$ the molar balance (eq. (10)) also includes the adsorption term.

$$(1 - \varepsilon_b) \xi_{ads} \varepsilon_{p,ads} \frac{\partial C_{ads,H_2O}}{\partial t} = a_{v,ads} k_{m,ads,H_2O} (C_{gas,H_2O} - C_{ads,H_2O}) - (1 - \varepsilon_b) \xi_{ads} \rho_{ads} \frac{\partial q}{\partial t} \tag{10}$$

The adsorbed $H_2O$ build up is estimated using the Linear Driving Force (LDF) approximation (eq. (11)), which also accounts for the internal mass transfer resistances:

$$\frac{\partial q}{\partial t} = K_{LDF} (q_{sat} - q) \tag{11}$$

The Danckwerts boundary conditions (eq. (12)) are imposed at the reactor inlet and outlet, along with symmetry and impermeability condition for the radial coordinate.

$$\begin{cases} F_{gas,i} = C^0_{gas,i} v^0_{gas} & z = 0 \\ F_{gas,tot} = C^0_{gas,tot} v^0_{gas} & z = 0 \\ C^0_{gas,i} = C_{gas,i} - \frac{D_{ae,i}}{v_{gas}} \frac{\partial C_{gas,i}}{\partial z} & z = 0 \\ \frac{\partial C_{gas,i}}{\partial z} = 0 & z = L_t \end{cases}$$

$$\frac{\partial C_{gas,i}}{\partial r} = 0 \quad r = 0$$

$$\frac{\partial C_{gas,i}}{\partial r} = 0 \quad r = d_t/2 \tag{12}$$

### 2.1.2. 2D dynamic energy balances

The energy balance of the gas phase (eq. (13)) consists of six terms: gas thermal capacity; axial thermal convection; radial and axial heat dispersion; heat transfer between the gas and the k-catalyst phases and heat exchange between the gas and adsorbent phase.

$$\varepsilon_b \rho_{gas} C_{p,gas} \frac{\partial T_{gas}}{\partial t} = -\rho_{gas} v_{gas} C_{p,gas} \frac{\partial T_{gas}}{\partial z} + \lambda_{rad} \left( \frac{\partial^2 T_{gas}}{\partial r^2} + \frac{1}{r} \frac{\partial T_{gas}}{\partial r} \right) + \lambda_{ax} \frac{\partial^2 T_{gas}}{\partial z^2} + \sum_k^{N_{cat}} a_{v,cat_k} h_{gs,cat_k} (T_{cat_k} - T_{gas}) + a_{v,ads} h_{gs,ads} (T_{ads} - T_{gas}) \tag{13}$$

The k-catalyst energy balance (eq. (14)) consists of three terms: catalyst thermal capacity; heat exchange between the gas and k-catalyst phase; enthalpy release by the reactions.

$$(1 - \varepsilon_b) \xi_{cat} \xi_k \rho_{cat_k} C_{p,cat_k} \frac{\partial T_{cat_k}}{\partial t} = a_{v,cat_k} h_{gs,cat_k} (T_{cat_k} - T_{gas}) + (1 - \varepsilon_b) \xi_{cat} \xi_k \rho_{cat_k} \sum_j^{N_R} -\Delta H_{r,j} R_{j,k}^{av} \tag{14}$$

The adsorbent energy balance (eq. (15)) consists of three terms: heat capacity; heat exchange between the gas and adsorbent phase; enthalpy release by the water adsorption.

$$(1 - \varepsilon_b) \xi_{ads} \rho_{ads} C_{p,ads} \frac{\partial T_{ads}}{\partial t} = a_{v,ads} h_{gs,ads} (T_{ads} - T_{gas}) + (1 - \varepsilon_b) \xi_{ads} \rho_{ads} \frac{\partial q}{\partial t} (-\Delta H_{ads}) \tag{15}$$

Danckwerts boundary conditions are used at reactor inlet and outlet, while symmetry condition and heat flux continuity at the wall are imposed on radial boundaries (Eq. (16)).

$$\begin{cases} T^0_{gas} = T_{gas} - \frac{\lambda_{ax}}{v_{gas} \rho_{gas} C_{p,gas}} \frac{\partial T_{gas}}{\partial z} & z = 0 \\ \frac{\partial T_{gas}}{\partial z} = 0 & z = L_t \end{cases}$$

$$\frac{\partial T_{gas}}{\partial r} = 0 \quad r = 0$$

$$\lambda_{rad} \frac{\partial T_{gas}}{\partial r} = h_w (T_{cool} - T_{gas}) \quad r = d_t/2 \tag{16}$$

### 2.1.3. 1D pseudo-stationary pellet mass balances

The i-species mass balances for the catalyst pellets are used to evaluate the effect of intraparticle diffusion limitations which have been reported to play a key role in DME synthesis process [32]. Assuming isothermal pellet and the pseudo-stationary conditions, the i-species mass balances (eq. (17)) consist of two terms accounting for the diffusion/reaction process. Two separate balances, one for each k-catalyst, are needed.

$$\frac{1}{x^2}\frac{\partial}{\partial x}\left(x^2 D_{eff,i}\rho_{gas}\frac{\partial C_{catk,int,i}}{\partial x}\right) + \rho_{cat,k}\sum_{j}^{N_R}\nu_{ij}R_{j,k} = 0 \quad (17)$$

The boundary conditions for the catalyst pellets (eq. (18)) are the symmetry condition at the particle center and imposed concentration, coherent with the solid catalyst phase mass balance (eq. (8)), at the particle external surface.

$$\frac{\partial C_{cat_{int},i}}{\partial x} = 0 \quad x = 0$$

$$C_{cat_{int},i} = C_{cat,i} \quad x = d_p/2 \quad (18)$$

The average reaction rates used in the balance equation are obtained by integrating the reaction rate profile inside the pellets (eq. (19)).

$$R_{j,k}^{av} = \frac{3\int_0^{r_p} R_{j,k}x^2 dx}{r_p^3} \quad (19)$$

### 2.2. Transport correlations, physical properties, reaction kinetic scheme and adsorption isotherm

The correlations used for heat and mass transport coefficients and mixture physical properties are reported in the *Supplementary materials - Section S1*. The correlations and parameters used are taken from the literature references [33–43].

The kinetic model used in the SEDMES reactor is a combination of the model proposed by Graaf et al. [44] for the methanol synthesis and the model of Ng et al. [45] for the methanol dehydration. The model considers the methanol synthesis from CO, the rWGS, the methanol synthesis from $CO_2$ and the methanol dehydration to DME with rate equations (20–23). Kinetic, adsorption and equilibrium constants, taken from ref. [44–47], are reported in *Supplementary materials - Section S2*. The fugacity coefficients used in the kinetics are calculated using the gPROMS® Multiflash 4.3 utility tool, which implements the Redlich-Kwong-Soave (RKS) equation of state. The products of fugacity coefficients ($K_{\Phi,j} = \prod_i \Phi_i^{\nu_{ij}}$) vary between 0.82 and 0.95 for the methanol synthesis reactions ($R_1$ and $R_3$), between 0.95 and 0.98 for the rWGS ($R_2$) and is very close to 1 for the methanol dehydration to DME ($R_4$).

$$R_1 = k_1\frac{K_{CO}(f_{CO}f_{H_2}^{3/2} - f_{CH_3OH}/(f_{H_2}^{1/2}K_{eq,1}))}{(1 + K_{CO}f_{CO} + K_{CO_2}f_{CO_2})(f_{H_2}^{1/2} + K_{H_2O/H_2}f_{H_2O})} \quad (20)$$

$$R_2 = k_2\frac{K_{CO_2}(f_{CO_2}f_{H_2} - f_{H_2O}f_{CO}/K_{eq,2})}{(1 + K_{CO}f_{CO} + K_{CO_2}f_{CO_2})(f_{H_2}^{1/2} + K_{H_2O/H_2}f_{H_2O})} \quad (21)$$

$$R_3 = k_3\frac{K_{CO_2}(f_{CO_2}f_{H_2}^{3/2} - f_{CH_3OH}f_{H_2O}/(f_{H_2}^{3/2}K_{eq,3}))}{(1 + K_{CO}f_{CO} + K_{CO_2}f_{CO_2})(f_{H_2}^{1/2} + K_{H_2O/H_2}f_{H_2O})} \quad (22)$$

$$R_4 = k_4\frac{K_{CH_3OH}^2 C_{CH_3OH}^2(1 - C_{H_2O}C_{CH_3OCH_3}/(C_{CH_3OH}^2 K_{eq,4}))}{(1 + 2\sqrt{K_{CH_3OH}C_{CH_3OH}} + K_{H_2O}C_{H_2O})^4} \quad (23)$$

The catalysts are homogeneously mixed with LTA zeolite 3A adsorbent. Water is considered as the only adsorbed component, due to the high affinity of the zeolite adsorbent. Gabruś et al. (2015) derived a Langmuir-Freundlich isotherm model for LTA zeolite 3A from adsorption equilibrium data at elevated temperatures (up to 250 °C) [23]. The adsorption model equations along with the corresponding parameters are reported in *Supplementary materials - Section S3*.

### 2.3. Numerical solution scheme

The mathematical SEDMES reactor model is implemented in gPROMS® software for the dynamic simulation. The standard solver 'DASOLV' for differential–algebraic equations systems based on implicit Backward Differentiation Formula (BDF) with variable time step and variable order is used for time integration. The integration time step of BDF changes in accordance with a maximum local error criterion implemented in gPROMS®. The BDF integration order is also automatically adjusted by the software algorithm varying from the first order (corresponding to an implicit Euler) to the fourth order. A first order Backward Finite Difference Method (BFDM) is used for the discretization of the axial reactor coordinate, instead, third order Orthogonal Collocations on Finite Elements Method (OCFEM) are used for the radial and the pellet coordinates. 60 discretization points are used along the axial coordinate in an equi-spaced grid, 2 finite elements for the radial coordinate and 2 for the pellet coordinate are used. The adequacy of the discretization grid was checked by a convergence analysis. The reporting time interval is 10 s.

## 3. Results and discussion

### 3.1. Model validation

The reactor model is validated by comparison with the experimental dynamic behavior during the adsorption/reaction step of a bench scale SEDMES tubular reactor (2 m length, 3.8 cm internal diameter) operated at the TNO test facilities in Petten. The reactor is loaded with a physical mixture of three different materials: cylindrical LTA zeolite 3A adsorbent, spherical CZA methanol synthesis and γ-alumina methanol dehydration catalysts. A sorbent to catalyst weight ratio of 4/1 and a MeOH to DME catalyst weight ratio of 1/1 are adopted. The physical properties of the solid phases (catalysts and sorbent) are reported in Table 1 [21,24,38,43,48]. Solid thermal conductivity is evaluated as a volume average of the properties of catalysts and sorbent phases. The geometrical parameters and operating conditions used as input (bench scale) in the simulation are reported in Table 2. The wall temperature, equal to the inlet temperature, is monitored over the length of the reactor and maintained at 525 K by electrical heating of the external metallic mass surrounding the reactor tube which guarantees a uniform (within ~ 2 K) external wall temperature. The reactor has been fed at a pressure of 25 bar, with GHSV = 100 $h^{-1}$ (referred to the total bed volume, which corresponds to 575 $h^{-1}$ referred to the catalyst volume) and a feed composition (Table 3) with a ratio $CO/CO_2$ = 0.5, a stoichiometric module M = ($H_2$-$CO_2$)/(CO + $CO_2$) = 2 and an inert $N_2$ content of 6.3%. At time zero the reactor is filled by a $N_2$ purge gas. The adsorption/reaction step lasts 2700 s.

Experiments in the SEDMES unit are performed under cyclic conditions, in which the adsorbent material is periodically regenerated removing the water from the adsorbent by PSA reducing the pressure to 1.5 bar and performing a countercurrent (with respect to the syngas feed) purge with inert gas. The initial water load after regeneration in the adsorbent material $q^0$ [$mol_{H2O}/kg_{ads}$] is not zero since the water is only partially removed: a fraction of the water adsorbed is still present in the zeolite and its amount at each reactor axial position must be evaluated. Therefore, the water loading profile at time zero is evaluated simulating a 4200 s countercurrent $N_2$ purge at 1.5 bar, GHSV 133 $h^{-1}$, wall temperature of 525 K, in line with the experimental regeneration

**Table 1**
Physical properties of solid phases.

| Parameter | Value | Unit |
|---|---|---|
| $\rho_{MeOH}$ | 1712 | [$kg/m^3$] |
| $\rho_{DME}$ | 1285 | [$kg/m^3$] |
| $\rho_{ads}$ | 1200 | [$kg/m^3$] |
| $C_{p,s}$ | 960 | [J/kg/K] |
| $\lambda_s$ | 0.22 | [W/m/K] |
| $\Delta H_{ads}$ | −45.95 | [$J/mol_{H2O}$] |

**Table 2**
Geometrical parameters and operating conditions of the reactor tube.

| Variable | Bench scale | Full scale | Unit |
|---|---|---|---|
| $L_t$ | 2 | 6 | [m] |
| $d_t$ | $3.8 \cdot 10^{-2}$ | $3.8 \cdot 10^{-2}$ | [m] |
| $d_{p,MeOHcat}$ | $2.4 \cdot 10^{-3}$ | $3 \cdot 10^{-3}$ | [m] |
| $d_{p,DMEcat}$ | $3.5 \cdot 10^{-3}$ | $3 \cdot 10^{-3}$ | [m] |
| $d_{pe,ads}$ | $3.2 \cdot 10^{-3}$ | $3.2 \cdot 10^{-3}$ | [m] |
| $\rho_{bed}$ | 800 | 800 | [kg/m$^3$] |
| Adsorbent/Catalystratio | 4/1 | 4/1 | [w/w] |
| MeOH/DMEcatalystratio | 1/1 | 1/1 | [w/w] |
| $T_g^0$ | 525 | 523 | [K] |
| $T_{cool}$ | 525 | 523 | [K] |
| $P^0$ | 25 | 25 | [bar] |
| GHSV | 100 | 140 | [$h^{-1}$] |

**Table 3**
Inlet feed composition in model validation.

| Compound | Molar fraction [%] |
|---|---|
| CO | 8.5 |
| $CO_2$ | 17.0 |
| $H_2$ | 68.2 |
| $N_2$ | 6.3 |

conditions.

The experimental data considered for comparison with model results are measured after an initial series of reaction-regeneration cycles in which the catalyst activity has levelled out, reaching stable conditions and showing a not significant deactivation. Standard mean deviations of experimental outlet molar fractions, evaluated from 5 subsequent cycles after stabilization, are 0.53% CO, 0.25% $CO_2$, 1.08% DME, 0.07% methanol.

The experimental outlet molar fraction of carbon containing species (CO, $CO_2$, $CH_3OH$ and DME) and the centerline temperature profile along the axial coordinate are used in the model validation. Experimental outlet molar composition is sampled with a time resolution of 294 s, while the temperatures are registered every 10 s, with seven equi-spaced thermocouples positioned between the reactor inlet and outlet. In this work only the measurements of the five internal thermocouples are considered since extremity effects not accounted by the model could markedly affect the closest temperatures to the inlet and outlet sections.

Multiplicative activity factors of the reaction rates are introduced in the literature equations (20–22) of methanol synthesis to grant a satisfactory model description of the bench scale experimental data. A reasonable match is obtained with an activity factors equal to 5 for the methanol synthesis reactions from CO and from $CO_2$ (rate equations (20) and (22)) and 7.5 for the rWGS reaction (rate equation (21)). Notably, activity factors higher than one have been reported for modern CZA catalysts for standard methanol synthesis [48]. This is likely associated with the progressive optimization of commercial catalyst formulations along the years. Besides it is expected that the specific SEDMES operating conditions, i.e. the very low concentration of water associated with the in-situ adsorption [18], could prevent the detrimental effect of $H_2O$ on catalyst stability [11,16], being responsible for a further increase of the standard reaction rates.

The comparison of model predictions with experimental outlet composition is reported in Fig. 1. At time zero the inlet feed to the reactor, which is full of inert purge gas, is step switched to the reacting mixture. For the first 8 min the composition at the reactor outlet does not change, then DME, mainly, and other products/reactants appear. The experimental breakthrough time of about 8 min due to the initial displacement of inert purge gas by reactants and products (including molar contraction associated with DME production) is well captured by the model. After the breakthrough DME is the most abundant species at the outlet, with an experimental trend well matched by the model showing a molar fraction peak of about 37% at about 1050 s. Then, the concentration of DME continuously decreases with time due to the progressive water hold up of the zeolite adsorbent. On the other hand, methanol outlet concentration, as correctly described by the model, is very low (below 1.5%) due to a combination of kinetic and thermodynamic factors associated with in-situ water removal, so the carbon selectivity to DME remains above 95%. After the breakthrough, consistently with the decrease in DME, both CO and $CO_2$ outlet concentrations continuously increase with time but with quite different dynamics. CO outlet molar fraction shows an initial increase with an almost asymptotic trend around 12%, while $CO_2$ concentration, which keeps very low due to the thermodynamic effect of $H_2O$ removal on rWGS equilibrium, is concave upward, indicating that steady state is not approached yet at the end of 2700 s adsorption/reaction step herein considered. Both these trends are qualitatively captured by the model, although some deviations from the experimental data are observed just after the breakthrough.

Simulation results also provide information about the way the reaction wave propagates through the catalyst bed of the SEDMES reactor, as shown in Fig. 2*a* by the time profiles of the DME specific flow rate at six different axial positions. All the profiles exhibit a similar trend: the flow rate of DME increases progressively when the reactants/products front reaches each position, raises to a maximum just after the local breakthrough and then decreases due to progressive increase of the local water loading on the zeolite material (Fig. 2*b*). Expectedly the maximum DME concentration becomes higher on moving along the axial coordinate due to the increasing extent of the synthesis reactions. The time lag of the DME breakthrough increases more than linearly with the distance from the reactor inlet. This is due to the strong molar contraction in the gas phase associated with the stoichiometries of DME production combined with in-situ water adsorption, which markedly decreases the volumetric flow rate along the reactor, making the purge gas displacement progressively slower.

The other key variable considered in the model validation is the time evolution of the gas centerline temperature. In Fig. 3 the experimental trajectories of centerline temperature in five axial locations are compared with the corresponding model predictions. Experimental data and simulation results show that the onset of temperature raising in the different location is coherent with the propagation of the reaction wave described in Fig. 2*a*. Upon being reached by the reaction front, the local

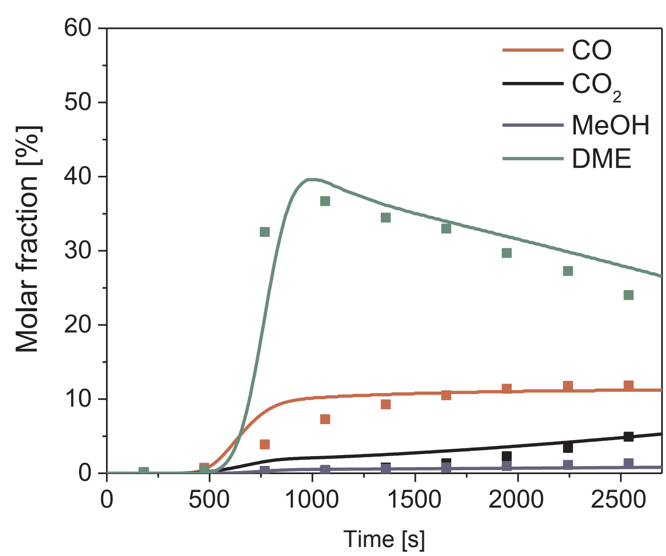


**Fig. 1.** Time evolution of outlet molar fraction experimental (■) vs. model (solid lines).

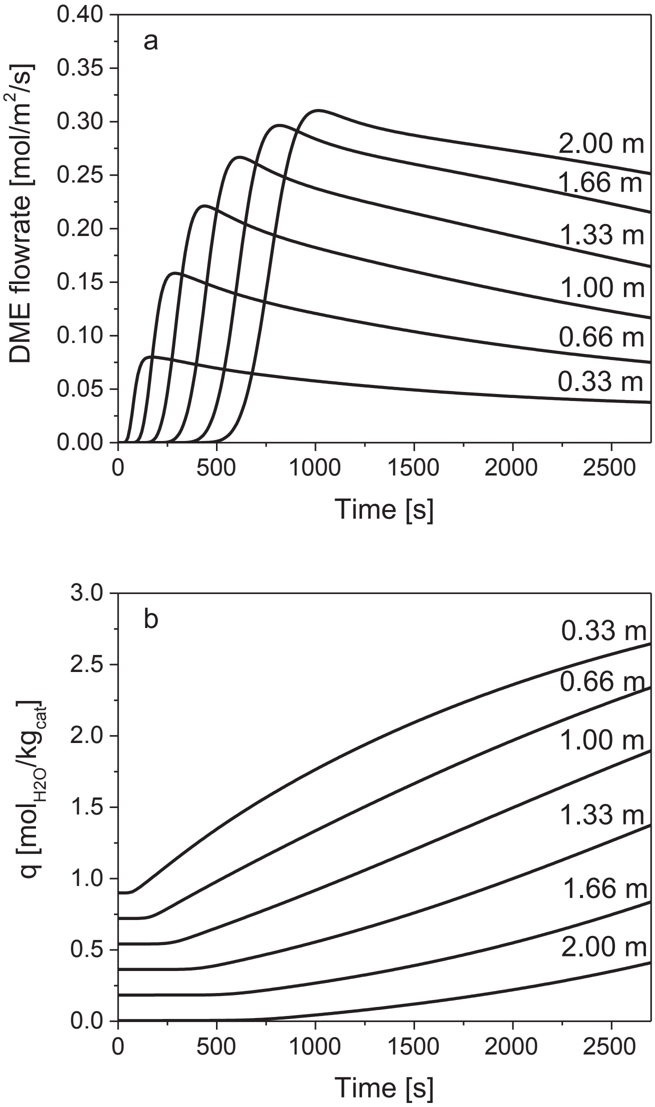


**Fig. 2.** Time evolution of a) outlet DME specific flow rate and b) adsorbed water load at different axial positions.

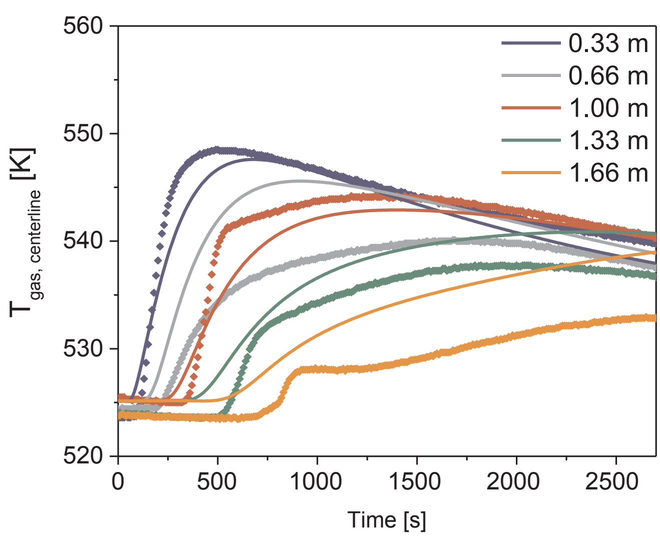


**Fig. 3.** Time evolution of centerline gas temperature at different reactor coordinates. Experimental (◆) vs. model (solid lines).

thermal dynamics is mainly governed by: i) heat release by exothermic reaction/adsorption process; ii) axial and radial heat transfer by convection and conduction; iii) heat capacity of the solid phases. The comparison of calculated profiles in Fig. 2*a* and Fig. 3 evidences that the maxima in the DME production wave correspond to the inflection point of temperature trajectories, the maximum temperature being reached after a significant time lag due to the dampening role of solid heat capacity. Simulation results match the experimental data reasonably well, particularly after the local maximum is reached, with the exception of the profile at 0.66 m (Fig. 3), which however is clearly an outlier as evidenced by internal comparison with the other experimental trajectories. Concerning detailed dynamic features, the experimental trajectories show steeper fronts than the calculated ones. A parameter sensitivity analysis shows that a better match can be obtained dividing the solid heat capacity by a factor of 3. However, a $C_p$ value of ~ 300 J/kg/K looks physically unrealistic for the considered solid materials. Besides, an increasing lag of the experimental temperature wave from the calculated one is observed moving from the inlet to the outlet of the reactor.

Nevertheless, the model is able to capture the catalyst temperature stress observed in the experiments, which is a key parameter in reactor design. The model can indeed describe the time evolution of temperature axial profiles as shown in Fig. 4*a* (reported with $\Delta t$ = 300 s) that can be used to evaluate the envelope of the maximum temperatures

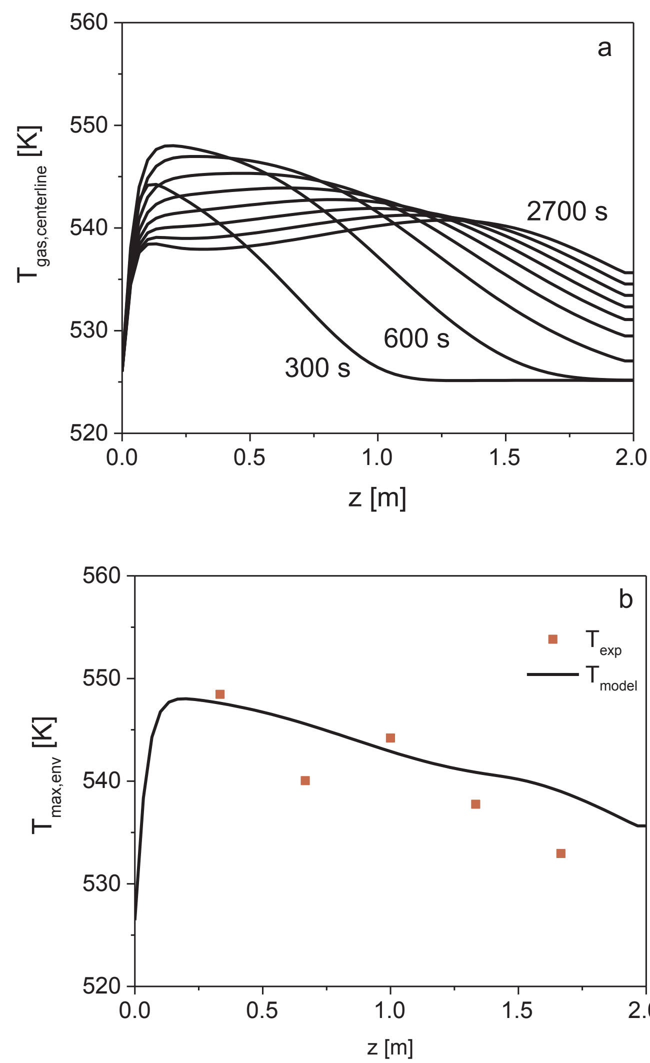


**Fig. 4.** a) Evolution of axial temperature profiles every 300 s b) Envelope of local maximum temperatures. Experimental (■) vs. model (solid line).

which is compared in Fig. 4*b* with the maximum values of temperature measured at the different axial locations during the adsorption/reaction step. The model predictions are well aligned with the experimental points, except for the outlier at 0.66 m, particularly in the first hotter part of the bed. It is worth noting that the deviations observed in the second half of the bed can be partly due to the not perfectly isothermal profile of the tube wall, which is slightly cooler in the downstream section as evidenced by the slight misalignment (2–3 °C) of the calculated from the experimental profiles before the breakthrough (Fig. 3).

The highest thermal stresses occurring close to the inlet section are related to the higher reaction (and adsorption) rates in the presence of the fresh reactants. Indeed, the envelope of local maximum temperatures resembles that of maximum reaction/adsorption heat release reported in Fig. 5. Inspection of Fig. 5 also shows that the contributions to the total enthalpy release from the catalytic reactions and $H_2O$ adsorption are almost equivalent, which is consistent with the similar contributions to enthalpy release in DME formation from $CO_2$ associated with the reaction ($\Delta H_{react}$ = -122 kJ/mol$_{DME}$) and the adsorption ($\Delta H_{ads}$ = -138 kJ/mol$_{DME}$, i.e. $\Delta H_{ads}$ = -46 kJ/mol$_{H2O}$) terms. Besides it is also evident the shoulder of the envelope of local maximum temperatures in the second half of the bed observed in Fig. 4 is associated with a similar trend of the $H_2O$ adsorption contribution, which is likely due to the initial $H_2O$ load profile of the sorbent, linearly increasing from the outlet to the inlet of the bed in the reaction/adsorption phase.

### 3.2. Industrial scale reactor analysis and design

The validated model is used for a parametric analysis of an externally cooled industrial scale SEDMES multitubular reactor (6 m length and 38 mm diameter tubes). The operating conditions and the reactor and catalyst parameters (full scale) are reported in Table 2. The reactor operates at 25 bar, 523 K as gas inlet and wall temperature, GHSV 140 $h^{-1}$. These input parameters are chosen according to the optimal operating conditions discussed in a previous paper of some of the authors [21], which addresses the cycle design by means of a 1D reactor model simulating the full SEDMES cycle. Specifically, temperature is chosen as a trade-off between kinetics and thermodynamics, pressure as a trade-off between thermodynamics and unsteady state operation costs and complexity, the space velocity is selected instead as a kinetic trade-off between the DME yield and productivity.

The reactor is loaded with a physical mixture of LTA adsorbent, CZA and γ-alumina catalysts. An adsorbent to catalyst ratio of 4:1 by weight is taken considering that the amount of adsorbent should guarantee effective water removal while keeping the amount of catalyst high enough to not kinetically limit the process [21]. A CZA to γ-alumina ratio of 1:1 by weight is taken as in model validation tests. Noteworthy, considering the different density of the solids involved and the overall GHSV used (140 $h^{-1}$), this corresponds to GHSV referred to the CZA catalyst volume of 1880 $h^{-1}$. A similar GHSV of 2000 $h^{-1}$ is reported to be the optimum for DME productivity in the conventional direct synthesis process with a mechanical mixture of CZA/γ-alumina [49], while, for a standard methanol synthesis reactor in a recycle loop [48], the GHSV is about 8000 $h^{-1}$ (2000 $h^{-1}$ when referred to the fresh feed flow rate assuming a recycle ratio around 3).

Concerning the cycle time, based on the 3-column design proposed in [21] a reaction/adsorption time, t = 3600 s has been set, followed by a 7200 s regeneration including blowdown, purge and repressurization. These values allow an effective control of water partial pressure at the reactor outlet during the adsorption/reaction step and an almost complete desorption of water from the zeolite during regeneration. Initial temperature and concentrations in the reactor, including the water load profile at time zero $q^0$ are evaluated simulating 5400 s of purging with an inert $N_2$ stream at 1.5 bar, GHSV = 250 $h^{-1}$, and wall temperature of 523 K.

#### 3.2.1. CO/CO$_2$ ratio effects

The effect of CO/$CO_2$ ratio is explored considering three cases (Table 4): a $CO_2$ rich condition with a CO/$CO_2$ ratio equal to 0.5 (the same used in model validation), an intermediate condition with equimolar CO and $CO_2$ content, that is typical of a syngas obtained from biomass gasification [14] and a CO rich conditions with a CO/$CO_2$ ratio equal to 2. The stoichiometric module M is taken equal to 2 which is the ideal value for SEDMES operation [21]. The same fraction of inert used in the model validation section is adopted.

Temporal profiles of the outlet flowrate of CO, $CO_2$ and overall $CO_x$, normalized with respect to the corresponding inlet flow, are shown in Fig. 6. The $CO_x$ flow rates are zero in the first part of the reaction/adsorption step until the breakthrough of the reactants/products stream front has replaced the initial inert gas used as starting condition (Fig. 6*a*). After the breakthrough the normalized outlet flow rate of CO is almost constant but its level changes significantly with the CO/$CO_2$ ratio: it decreases from about 50% with $CO_2$ rich feed to about 20% with CO rich feed. In SEDMES indeed, the water adsorption shifts the rWGS equilibrium, partially converting $CO_2$ to CO, resulting in a lower apparent CO conversion when using a $CO_2$ rich feed. The situation is the opposite for the $CO_2$ normalized outlet flow, that slightly increases with the $CO_2$ feed content, and grows monotonously with time, coherently with the progressive $H_2O$ hold up on the adsorbent material.

Noteworthy, the resulting overall $CO_x$ profiles (Fig. 6*b*) are poorly sensitive on feed compositions in the first part of the reaction/adsorption phase, while faster hold up of the sorbent due to the higher generation of water results in a steeper increase of normalized $CO_x$ flow rate with time in the presence of $CO_2$ rich feed. This can be explained on the basis of the overall process stoichiometries, considering CO or $CO_2$ as carbon source, reported in equation (24) and (25), respectively.

$$2CO + 4H_2 \leftrightarrow CH_3OCH_3 + H_2O \downarrow_{ads} \quad \Delta H_r^0 = -250.0 \text{kJ/mol} \tag{24}$$

$$2CO_2 + 6H_2 \leftrightarrow CH_3OCH_3 + 3H_2O \downarrow_{ads} \quad \Delta H_r^0 = -259.7 \text{kJ/mol} \tag{25}$$

The moles of water produced per mole of DME starting from $CO_2$ are three times higher than those produced using CO as carbon source. Consequently, the water loading in the adsorbent material is larger in $CO_2$ rich case as shown in Fig. 7. The amount of adsorbed water increases significantly when passing from a CO/$CO_2$ ratio 2 to 0.5. However, the water loading profiles after 3600 s have the same shape in all the three cases in analysis: there is a maximum at around 1 m from the reactor inlet and the loading decreases while moving along the axial coordinate, in accordance to the progression of the reaction/adsorption front. This means that for $CO_2$ rich syngas feed (e.g. those obtained

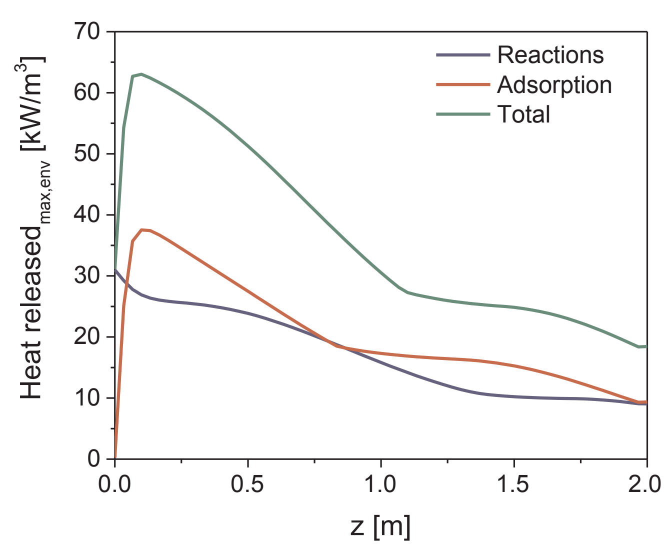


**Fig. 5.** Envelope of local maximum reaction/adsorption heat release.

**Table 4**
Inlet feed composition in industrial scale reactor analysis.

| Compound | $CO_2$ rich | Intermediate | CO rich | Unit |
|---|---|---|---|---|
| CO | 8.5 | 13.4 | 18.7 | [%] |
| $CO_2$ | 17 | 13.4 | 9.4 | [%] |
| $H_2$ | 68.2 | 66.9 | 65.6 | [%] |
| $N_2$ | 6.3 | 6.3 | 6.3 | [%] |

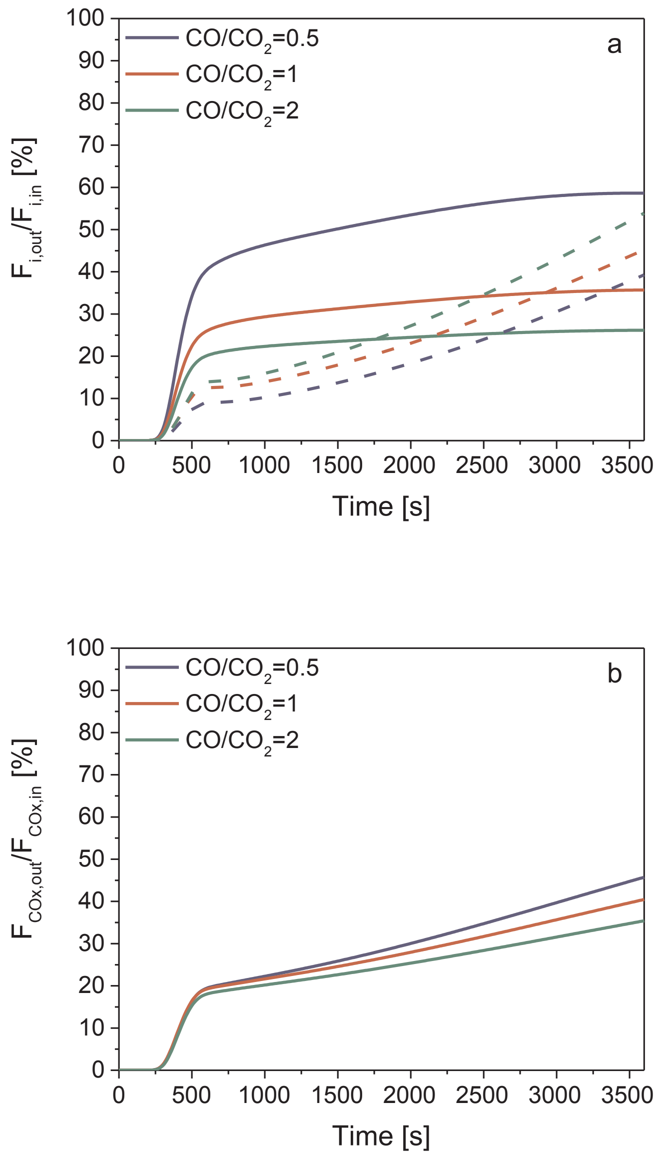


**Fig. 6.** Time evolution of the dimensionless flowrate for carbon containing reactants at different $CO/CO_2$ feed ratios. a) CO (solid lines) and $CO_2$ (dashed lines) flow rate out/in ratios; b) Total $CO_x$ flow rate out/in ratio.

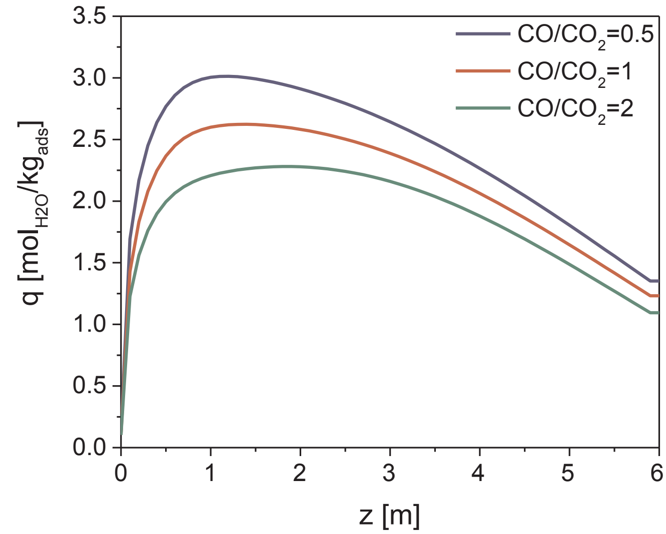


**Fig. 7.** Axial profile of the average (on cross section area) adsorbent water load profile at time 3600 s for different feed $CO/CO_2$ ratios.

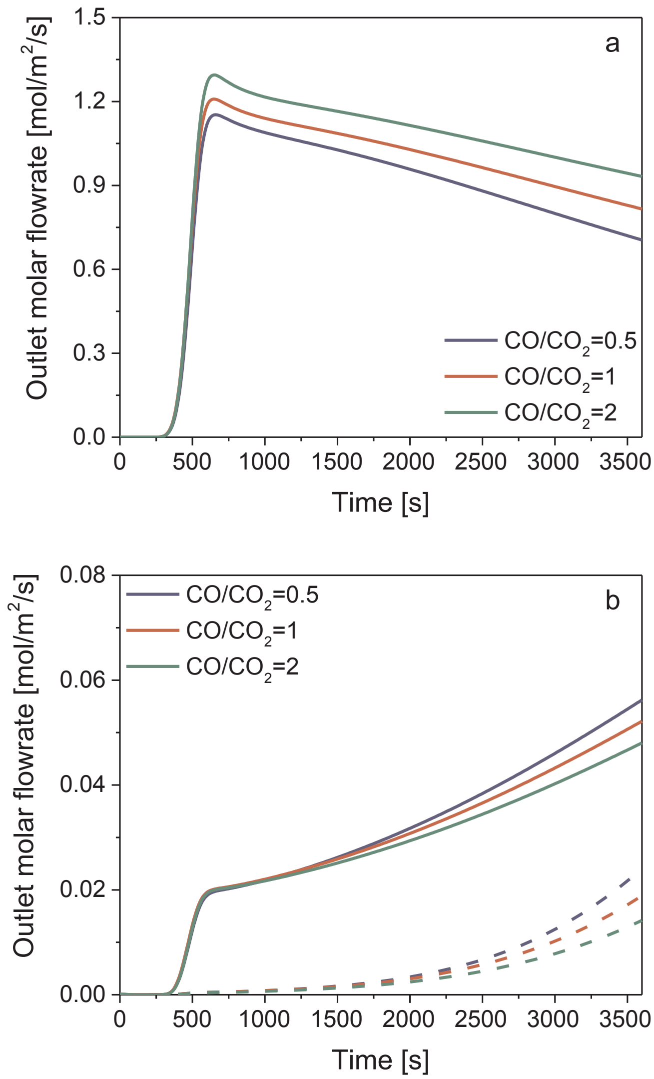


**Fig. 8.** Time evolution of outlet product flowrate per unit area at different $CO/CO_2$ ratios. a) DME outlet flowrate; b) methanol (solid lines) and water (dashed lines) flowrates.

from biomass [14]) reactors with a larger adsorbent/catalyst ratio or with more frequent regeneration steps must be employed in order to guarantee an effective in-situ water removal. This is mainly addressed by cycle design and its optimization [21].

The time evolution of the outlet specific flowrate of the reaction products (DME, methanol and water) is reported in Fig. 8: the DME profiles are shown in Fig. 8*a*, while the methanol and water profiles are shown in Fig. 8*b*. As expected, the shape of DME flowrate profiles is similar to that observed in the validation testing (Fig. 2*a)*. The outlet flowrate of DME steeply increases just after the breakthrough, reaches a maximum between 600 and 700 s, and then slowly decreases due to the progressive $H_2O$ hold up on the adsorbent material. The production of DME slightly increases with the CO content in the feed, in all the time range after the breakthrough. The carbon selectivity to DME is particularly high, the outlet flow rate of methanol being almost two order of magnitude smaller than the DME one.

The methanol flowrate is very similar for all the $CO/CO_2$ ratios, and its onset is related to the progressive hold up of the sorbent and the consequent increase of water outlet concentration (Fig. 8*b)*, which progressively shifts back the Methanol/DME dehydration equilibrium. It is worth noticing that, in the case of CO rich feed, the higher production of DME is partly due to the larger amount of carbon fed to the system, since the stoichiometric module M has been maintained equal to 2 in all the simulations.

In order to better assess the efficiency of SEDMES to convert carbon to DME, the DME flowrate profiles have been normalized with respect to the effective carbon content in the feed. Accordingly, the parameter $F^*_{C\rightarrow DME}$ has been defined as reported in equation (26).

$$F^*_{C\rightarrow DME} = \frac{2F_{DME_{out}}}{(F_{CO} + F_{CO_2})_{in}} \tag{26}$$

The profiles in Fig. 9 show clearly that, in SEDMES, the efficiency in the conversion of carbon to DME is almost independent on the $CO/CO_2$ feed ratio, as already reported in previous studies of some of the authors [18,21]. This is consistent with the evidence that $CO_x$ conversion is the same for any $CO/CO_2$ ratio and that the selectivity to DME is always extremely high (the maximum methanol selectivity calculated in the simulations below 4%). The $F^*_{C\rightarrow DME}$ profiles obtained for different $CO/CO_2$ feed ratios show slight differences only in the last part of the reaction/adsorption step due to the already mentioned faster water production in $CO_2$ rich case and the consequent increase of water content in the reaction environment.

Notably, in SEDMES, the DME carbon yield cannot be calculated as in a conventional steady state process and should be evaluated as the time integral of inlet and outlet flows along the full SEDMES process cycle (reaction/adsorption and regeneration steps). Since the regeneration steps of the cycle were not simulated in this work, an approximation of the overall DME carbon yield has been obtained with equation (27) under the assumptions that reactions are frozen during the blow down step and that all the DME present in the reactor at the end of the reaction/adsorption step is recovered. Equation (27) accounts for both the DME flowing out during the reaction/adsorption step plotted in Fig. 8 and Fig. 9 and the amount of DME which is present in the reactor at the end of the step (i.e. the blowdown/depress product).

$$Y_{DME} = 2\frac{(\int_0^{t_{end}} F_{DME_{out}}\,dt + \int_0^{V_t} C_{gas,DME}(t_{end})dV_t)}{\int_0^{t_{end}} (F_{CO_{in}} + F_{CO_{2_{in}}})dt} \tag{27}$$

The calculated values of DME yield, $Y_{DME}$, are reported in Table 5, together with the equilibrium yields expected in the conventional direct DME synthesis. The yield values for these cases are in line with those already reported in previous studies [21]. Note that the experiments considered here relate to dedicated experiments for studying SEDMES reactor performance and are not aimed at cycle optimization. These results confirm that SEDMES is poorly sensitive on the $CO/CO_2$ ratio in the feed , the difference in DME yield between CO rich and $CO_2$ rich conditions being less than 6%, as already evidenced by the small gap between the profiles plotted in Fig. 9 after ~ 1500 s. In contrast, the equilibrium DME carbon yield, i.e. the maximum yield obtainable in conventional direct synthesis processes, markedly changes on varying the $CO/CO_2$ feed ratio. In line with previous results [21], it can be concluded that the advantage of using SEDMES is especially large for higher $CO_2$ feed content. The yield improvement achieved by SEDMES with respect to equilibrium values for the conventional direct synthesis of DME (see *Supplementary materials - Section S4*) increases from 26.8% with CO rich feed to 37.4% $CO_2$ rich feed for the evaluated cases. Due to its dynamic nature the SEDMES process has more degrees of freedom in optimizing the DME yield than the conventional synthesis, as described in [21], allowing even higher yields for all feed conditions than reported here.

Looking at the thermal behavior of the SEDMES reactor, the envelope of the maximum temperatures achieved in each axial coordinate is reported in Fig. 10 for different $CO/CO_2$ feed ratios. As observed in the validation section, the inlet zone is the most thermally stressed part of the reactor, due to the higher heat release associated with the rapid conversion of the fresh reactants and the adsorption of the produced water. The peak is slightly higher in the case of CO rich feed. This is exclusively due to kinetic factors, which results in the faster production of DME in the inlet zone in the case of CO rich feed, consistently with the higher DME outlet flow rate shown in Fig. 8. Indeed, when accounting for the heat released by water adsorption, the synthesis of DME from CO and from $CO_2$ are almost equally exothermic (eq. (24) and (25)). It is worth noting that in the most severe case, the temperature is comparable to the conventional direct DME synthesis [50], despite of the additional contribution of the exothermic water adsorption. This is due to the dilution of catalyst by the sorbent material, which is present in large amount inside the reactor tube (4/1 w/w).

### 3.2.2. Tube diameter effects

The effect of tube diameter is investigated considering tubes with internal diameters equal to 25.6 mm (O.D. 1.25 in., B.W.G. gage 11), 38 mm and 46.6 mm (O.D. 2 in., B.W.G. gage 14). The other input parameters are the same to those already given in Table 2, with the intermediate composition ($CO/CO_2 = 1$) in Table 4.

The calculated envelope of maximum gas temperature profiles in the cross-section centerline are reported in Fig. 11. As expected, the temperature control is much easier with smaller tubes that can exchange better the heat generated by reaction and adsorption: it is straightforward that the larger the tubes are, the higher are the maximum temperatures. However, it is important to notice that, thanks to the dilution of the catalyst by the sorbent, the differences among the three simulated profiles are not so drastic, and even with the largest diameter (46.6 mm) the temperature control is not a critical issue (less than 10 K difference at any position along the axial coordinate, with a maximum temperature of 553 K). This is a key difference with the conventional DME direct synthesis, which usually requires tubes with smaller internal diameters (3 cm diameter in reference [51]) to avoid hot-spots exceeding the catalyst temperature limit.

The temperature difference has no strong effect on the DME

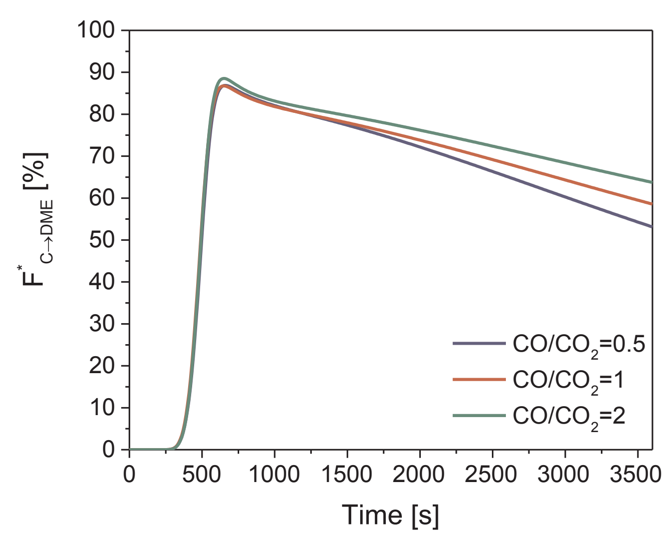


**Fig. 9.** Time evolution of outlet DME flowrate normalized with respect to inlet carbon flow rate at different feed $CO/CO_2$ ratios.

**Table 5**
DME carbon yield at different $CO/CO_2$ feed ratios.

| | $CO_2$ rich | Intermediate | CO rich | Unit |
|---|---|---|---|---|
| SEDMES | 64.9 | 67.6 | 70.7 | [%] |
| Equilibrium | 27.5 | 35.4 | 43.9 | [%] |

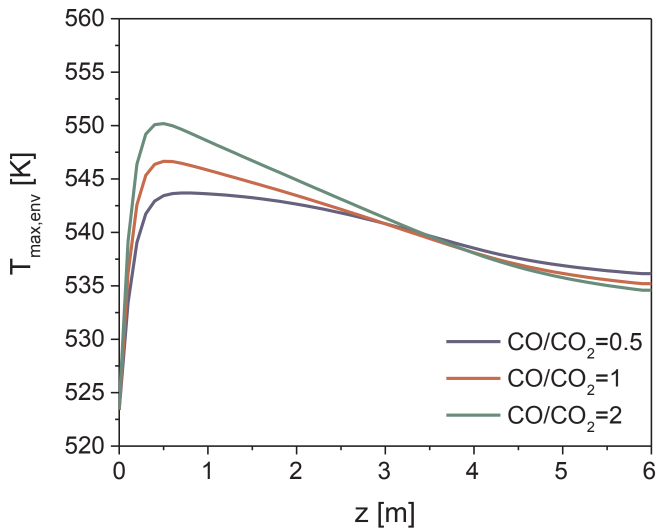


**Fig. 10.** Axial profile of envelope of maximum gas centreline local temperatures at different feed $CO/CO_2$ ratios.

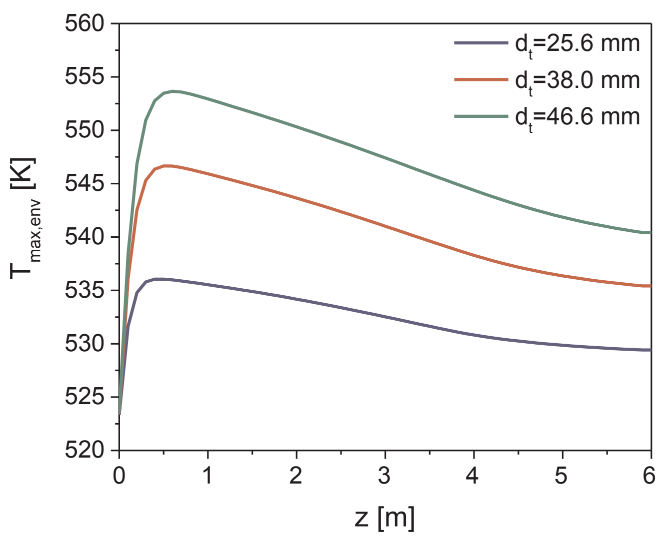


**Fig. 11.** Axial profile of maximum gas centreline local temperatures with different tube diameters.

production, as shown in Fig. 12 where the specific outlet flow rates of DME have been plotted. Only a slightly higher peak of DME flow rate is observed with larger diameters just after the breakthrough at ~ 500 s, while the opposite situation is observed on the long term (after ~ 1100 s), when the production of DME is higher with a smaller tube diameter. This is a consequence of the temperature effects on chemical kinetics and water adsorption equilibria, respectively. Just after the DME breakthrough the higher temperature in large tubes enhances the reaction kinetics, increasing the reactant conversion to DME; afterwards the lower temperature allowed by small diameter tubes becomes progressively beneficial due to its positive effect on the water adsorption equilibrium with a consequent DME production improvement.

The DME carbon yields, calculated as according to equation (27) in the composition analysis, are reported in Table 6. There are no wide differences, DME yield decreasing less than 2.5% passing from an internal diameter of 25.6 mm to 46.6 mm. The small yield performance improvement obtained using smaller tubes is given, on long term, by the thermodynamic increase in the water adsorption capacity [23], which, as shown in Fig. 12, leads to an increase in the DME production.

## 4. Conclusions

The thermal behavior and the DME yield performances of a SEDMES bench scale and industrial scale reactors are investigated by means of a 2D + 1D model of the reaction/adsorption step in a single tube of the fixed bed converter.

The model is validated by comparison with the experimental results obtained in a bench scale unit, showing the ability to capture the dynamics of the outlet composition and to describe the evolution of the catalyst temperature stress along the axial reactor coordinate.

The effect of the $CO/CO_2$ ratio in the feed is addressed, confirming that, thanks to the effective in-situ $H_2O$ removal, the DME yield performances of sorption enhanced processes are poorly sensitive on the $CO/CO_2$ ratio: the difference in DME yield after a 3600 s reaction/adsorption step in the case of a rich $CO_2$ feed ($CO/CO_2$ = 0.5) and a lean $CO_2$ feed ($CO/CO_2$ = 2) is less than 6% (64.9% vs. 70.7%). Accordingly, at high $CO_2$ content in the feed, the SEDMES process provides increasing advantage with respect to the conventional direct synthesis of DME, that shows a yield difference of 16.4% between the mentioned cases (27.5% vs. 43.9%).

The envelope of maximum temperatures achieved along the axial coordinate shows that catalyst thermal stresses in the hotter inlet zone of the reactor slightly increase with the CO content in the feed (reaching 550 K with $CO/CO_2$ = 2) with due to faster kinetics of the DME production reactions. However, thanks to the dilution effect provided by the adsorption material (catalyst:adsorbent = 1:4 w/w), maximum bed temperature keeps well below the limits reported in the literature (573 K) to preserve the CZA catalyst stability. Accordingly, larger tube diameters (up to 46.6 mm) than in conventional DME direct synthesis reactor can be adopted with less than 2% loss in DME yield.

## Declaration of Competing Interest

The authors declare that they have no known competing financial interests or personal relationships that could have appeared to

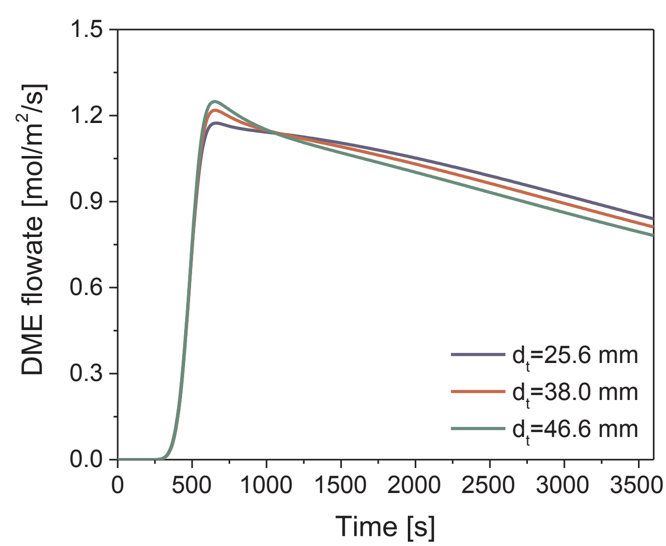


**Fig. 12.** Time evolution of outlet DME flow rate per unit area with different tube diameters.

**Table 6**
DME carbon yield with different tube diameters.

| | $d_t$ = 25.6 mm | $d_t$ = 38.0 mm | $d_t$ = 46.6 mm | Unit |
|---|---|---|---|---|
| SEDMES | 68.6 | 67.6 | 66.2 | [%] |

influence the work reported in this paper.

## Acknowledgements

This work has received funding from the European Union's Horizon 2020 research and innovation programme under grant agreement No. 727600.

## Appendix A. Supplementary data

Supplementary data to this article can be found online at https://doi.org/10.1016/j.cej.2020.126573.

## References

[1] T.A. Semelsberger, R.L. Borup, H.L. Greene, Dimethyl ether (DME) as an alternative fuel, J. Power Sources 156 (2006) 497–511, https://doi.org/10.1016/j.jpowsour.2005.05.082.
[2] R. Anggarani, C.S. Wibowo, D. Rulianto, Application of dimethyl ether as LPG substitution for household stove, Energy Procedia 47 (2014) 227–234, https://doi.org/10.1016/j.egypro.2014.01.218.
[3] S. Bhattacharya, K.B. Kabir, K. Hein, Dimethyl ether synthesis from Victorian brown coal through gasification - Current status, and research and development needs, Prog. Energy Combust. Sci. 39 (2013) 577–605, https://doi.org/10.1016/j.pecs.2013.06.003.
[4] C. Arcoumanis, C. Bae, R. Crookes, E. Kinoshita, The potential of di-methyl ether (DME) as an alternative fuel for compression-ignition engines: A review, Fuel 87 (2008) 1014–1030, https://doi.org/10.1016/j.fuel.2007.06.007.
[5] D. Cocco, V. Tola, G. Cau, Performance evaluation of chemically recuperated gas turbine (CRGT) power plants fuelled by di-methyl-ether (DME), Energy 31 (2006) 1446–1458, https://doi.org/10.1016/j.energy.2005.05.015.
[6] T.A. Semelsberger, K.C. Ott, R.L. Borup, H.L. Greene, Generating hydrogen-rich fuel-cell feeds from dimethyl ether (DME) using physical mixtures of a commercial Cu/Zn/Al2O3 catalyst and several solid-acid catalysts, Appl. Catal. B Environ. 65 (2006) 291–300, https://doi.org/10.1016/j.apcatb.2006.02.015.
[7] K. Klier, Methanol synthesis, Adv. Catal. 31 (1982) 243–313, https://doi.org/10.1016/S0360-0564(08)60455-1.
[8] J.J. Spivey, Review: Dehydration catalysts for the methanol/dimethyl ether reaction, Chem. Eng. Commun. 110 (1991) 123–142, https://doi.org/10.1080/00986449108939946.
[9] D. Song, W. Cho, D.K. Park, E.S. Yoon, Comparison of the performance of a fixed bed reactor in the two cases, mixture of catalyst pellets and a hybrid catalyst, for dimetyl ether synthesis, J. Ind. Eng. Chem. 13 (2007) 815–826.
[10] K. Saravanan, H. Ham, N. Tsubaki, J.W. Bae, Recent progress for direct synthesis of dimethyl ether from syngas on the heterogeneous bifunctional hybrid catalysts, Appl. Catal. B Environ. 217 (2017) 494–522, https://doi.org/10.1016/j.apcatb.2017.05.085.
[11] F. Dadgar, R. Myrstad, P. Pfeifer, A. Holmen, H.J. Venvik, Direct dimethyl ether synthesis from synthesis gas: The influence of methanol dehydration on methanol synthesis reaction, Catal. Today 270 (2016) 76–84, https://doi.org/10.1016/j.cattod.2015.09.024.
[12] A. Hankin, N. Shah, Process exploration and assessment for the production of methanol and dimethyl ether from carbon dioxide and water, Sustain. Energy Fuels. 1 (2017) 1541–1556, https://doi.org/10.1039/c7se00206h.
[13] G. Jia, Y. Tan, Y. Han, A comparative study on the thermodynamics of dimethyl ether synthesis from CO hydrogenation and CO2 hydrogenation, Ind. Eng. Chem. Res. 45 (2006) 1152–1159, https://doi.org/10.1021/ie050499b.
[14] I. Martínez, V. Kulakova, G. Grasa, R. Murillo, Experimental investigation on sorption enhanced gasification (SEG) of biomass in a fluidized bed reactor for producing a tailored syngas, Fuel 259 (2020) 116252, , https://doi.org/10.1016/j.fuel.2019.116252.
[15] M. De Falco, M. Capocelli, G. Centi, Dimethyl ether production from CO2 rich feedstocks in a one-step process: Thermodynamic evaluation and reactor simulation, Chem. Eng. J. 294 (2016) 400–409, https://doi.org/10.1016/j.cej.2016.03.009.
[16] M.B. Fichtl, D. Schlereth, N. Jacobsen, I. Kasatkin, J. Schumann, M. Behrens, R. Schlögl, O. Hinrichsen, Kinetics of deactivation on Cu/ZnO/Al2O3 methanol synthesis catalysts, Appl. Catal. A Gen. 502 (2015) 262–270, https://doi.org/10.1016/j.apcata.2015.06.014.
[17] J. Boon, J. van Kampen, R. Hoogendoorn, S. Tanase, F.P.F. van Berkel, M. van Sint Annaland, Reversible deactivation of γ-alumina by steam in the gas-phase dehydration of methanol to dimethyl ether, Catal. Commun. 119 (2019) 22–27, https://doi.org/10.1016/j.catcom.2018.10.008.
[18] J. van Kampen, J. Boon, F. van Berkel, J. Vente, M. van Sint Annaland, Steam separation enhanced reactions: Review and outlook, Chem. Eng. J. 374 (2019) 1286–1303, https://doi.org/10.1016/j.cej.2019.06.031.
[19] I. Iliuta, F. Larachi, P. Fongarland, Dimethyl ether synthesis with in situ H2O removal in fixed-bed membrane reactor: Model and simulations, Ind. Eng. Chem. Res. 49 (2010) 6870–6877, https://doi.org/10.1021/ie901726u.
[20] I. Iliuta, M.C. Iliuta, F. Larachi, Sorption-enhanced dimethyl ether synthesis-Multiscale reactor modeling, Chem. Eng. Sci. 66 (2011) 2241–2251, https://doi.org/10.1016/j.ces.2011.02.047.
[21] J. van Kampen, J. Boon, J. Vente, M. van Sint Annaland, Sorption enhanced dimethyl ether synthesis for high efficiency carbon conversion: Modelling and cycle design, J. CO2 Util. 37 (2020) 295–308, https://doi.org/10.1016/j.jcou.2019.12.021.
[22] A. Gorbach, M. Stegmaier, G. Eigenberger, Measurement and modeling of water vapor adsorption on zeolite 4A - Equilibria and kinetics, Adsorption 10 (2004) 29–46, https://doi.org/10.1023/B:ADSO.0000024033.60103.ff.
[23] E. Gabruś, J. Nastaj, P. Tabero, T. Aleksandrzak, Experimental studies on 3A and 4A zeolite molecular sieves regeneration in TSA process: Aliphatic alcohols dewatering-water desorption, Chem. Eng. J. 259 (2015) 232–242, https://doi.org/10.1016/j.cej.2014.07.108.
[24] M. Simo, S. Sivashanmugam, C.J. Brown, V. Hlavacek, Adsorption/desorption of water and ethanol on 3A zeolite in near-adiabatic fixed bed, Ind. Eng. Chem. Res. 48 (2009) 9247–9260, https://doi.org/10.1021/ie900446v.
[25] B.T. Carvill, J.R. Hufton, M. Anand, S. Sircar, Sorption-Enhanced Reaction Process, AIChE J. 42 (1996) 2765–2772, https://doi.org/10.1002/aic.690421008.
[26] S. Walspurger, G.D. Elzinga, J.W. Dijkstra, M. Sarić, W.G. Haije, Sorption enhanced methanation for substitute natural gas production: Experimental results and thermodynamic considerations, Chem. Eng. J. 242 (2014) 379–386, https://doi.org/10.1016/j.cej.2013.12.045.
[27] A. Borgschulte, N. Gallandat, B. Probst, R. Suter, E. Callini, D. Ferri, Y. Arroyo, R. Erni, H. Geerlings, A. Züttel, Sorption enhanced CO2 methanation, PCCP 15 (2013) 9620–9625, https://doi.org/10.1039/c3cp51408k.
[28] J. Terreni, M. Trottmann, T. Franken, A. Heel, A. Borgschulte, Sorption-Enhanced Methanol Synthesis, Energy Technol. 7 (2019) 1–9, https://doi.org/10.1002/ente.201801093.
[29] A. Zachopoulos, E. Heracleous, Overcoming the equilibrium barriers of CO2 hydrogenation to methanol via water sorption: A thermodynamic analysis, J. CO2 Util. 21 (2017) 360–367, https://doi.org/10.1016/j.jcou.2017.06.007.
[30] H.J. Kim, H. Jung, K.Y. Lee, Effect of Water on Liquid Phase DME Synthesis from Syngas over Hybrid Catalysts Composed of Cu/ZnO/Al2O3 and γ-Al2O3, Korean J. Chem. Eng. 18 (2001) 838–841, https://doi.org/10.1007/BF02705605.
[31] M.V. Twigg, M.S. Spencer, Deactivation of supported copper metal catalysts for hydrogenation reactions, Appl. Catal. A Gen. 212 (2001) 161–174, https://doi.org/10.1016/S0926-860X(00)00854-1.
[32] S. Guffanti, C.G. Visconti, G. Groppi, A model analysis of the effects of active phase distribution at the pellet scale in catalytic reactors for the direct dimethyl ether synthesis, Ind. Eng. Chem. Res. (2020), https://doi.org/10.1021/acs.iecr.0c01938.
[33] N. Wakao, T. Funazkri, Effect of fluid dispersion coefficients on particle-to-fluid mass transfer coefficients in packed beds. Correlation of sherwood numbers, Chem. Eng. Sci. 33 (1978) 1375–1384, https://doi.org/10.1016/0009-2509(78)85120-3.
[34] V. Specchia, S. Sicardi, Modified correlation for the conductive contribution of thermal conductivity in packed bed reactors, Chem. Eng. Commun. 6 (1980) 131–139, https://doi.org/10.1080/00986448008912525.
[35] V. Specchia, G. Baldi, S. Sicardi, Heat transfer in packed bed reactors with one phase flow, Chem. Eng. Commun. 4 (1980) 361–380, https://doi.org/10.1080/00986448008935916.
[36] R. Pfeffer, Heat and mass transport in multiparticle systems, Ind. Eng. Chem. Fundam. 3 (1964) 380–383, https://doi.org/10.1021/i160012a018.
[37] G.H. Graaf, H. Scholtens, E.J. Stamhuis, A.A.C.M. Beenackers, Intra-particle diffusion limitations in low-pressure methanol synthesis, Chem. Eng. Sci. 45 (1990) 773–783, https://doi.org/10.1016/0009-2509(90)85001-T.
[38] E. Gabruś, K. Witkiewicz, J. Nastaj, Modeling of regeneration stage of 3A and 4A zeolite molecular sieves in TSA process used for dewatering of aliphatic alcohols, Chem. Eng. J. 337 (2018) 416–427, https://doi.org/10.1016/j.cej.2017.12.112.
[39] E.N. Fuller, K. Ensley, J.C. Giddings, Diffusion of halogenated hydrocarbons in helium. The effect of structure on collision cross sections, J. Phys. Chem. 73 (1969) 3679–3685, https://doi.org/10.1021/j100845a020.
[40] A.G. Dixon, Correlations for wall and particle shape effects on fixed bed bulk voidage, Can. J. Chem. Eng. 66 (1988) 705–708, https://doi.org/10.1002/cjce.5450660501.
[41] K.R. Cox, W.G. Chapman, The Properties of Gases and Liquids, 5th Edition, 2001.
[42] C. H. Bosanquet, British TA Report BR-507, 1944.
[43] G. Bercic, J. Levec, Intrinsic and global reaction rate of methanol dehydration over γ-Al2O3 pellets, Ind. Eng. Chem. Res. 31 (1992) 1035–1040.
[44] G.H. Graaf, E.J. Stamhuis, A.A.C.M. Beenackers, Kinetics of low-pressure methanol synthesis, Chem. Eng. Sci. 43 (1988) 3185–3195, https://doi.org/10.1016/0009-2509(88)85127-3.
[45] K.L. Ng, D. Chadwick, B.A. Toseland, Kinetics and modelling of dimethyl ether synthesis from synthesis gas, Chem. Eng. Sci. 54 (1999) 3587–3592, https://doi.org/10.1016/S0009-2509(98)00514-4.
[46] G.H. Graaf, P.J.J. Sijtsema, E.J. Stamhuis, G.E.H. Joosten, Chemical equilibria in methanol synthesis, Chem. Eng. Sci. 41 (1986) 2883–2890.
[47] W.Z. Lu, L.H. Teng, W. De Xiao, Simulation and experiment study of dimethyl ether synthesis from syngas in a fluidized-bed reactor, Chem. Eng. Sci. 59 (2004) 5455–5464, https://doi.org/10.1016/j.ces.2004.07.031.

[48] A. Montebelli, C.G. Visconti, G. Groppi, E. Tronconi, C. Ferreira, S. Kohler, Enabling small-scale methanol synthesis reactors through the adoption of highly conductive structured catalysts, Catal. Today 215 (2013) 176–185, https://doi.org/10.1016/j.cattod.2013.02.020.

[49] S.H. Lee, C. Wonjun, K.P. Dal, E.S. Yoon, Simulation of fixed bed reactor for dimethyl ether synthesis, Korean J. Chem. Eng. 23 (2006) 522–530, https://doi.org/10.1007/BF02706789.

[50] R. Peláez, P. Marín, F.V. Díez, S. Ordóñez, Direct synthesis of dimethyl ether in multi-tubular fixed-bed reactors: 2D multi-scale modelling and optimum design, Fuel Process. Technol. 174 (2018) 149–157, https://doi.org/10.1016/j.fuproc.2018.02.025.

[51] D. Song, W. Cho, G. Lee, D.K. Park, E.S. Yoon, Numerical analysis of a pilot-scale fixed-bed reactor for dimethyl ether (DME) synthesis, Ind. Eng. Chem. Res. 47 (2008) 4553–4559, https://doi.org/10.1021/ie071589e.